Paper

EFFECT OF RESPIRATORY MOTION ON LUNG COUNTING EFFICIENCY USING A 4D NURBS-BASED CARDIO-TORSO (NCAT) PHANTOM

Marilyn Tremblay,* Gary H. Kramer,* Kevin Capello,* and Paul Segars†

Abstract—**The Human Monitoring Laboratory (Canada) has looked at parameters (lung volume, lung deposition pattern, etc.) that can affect the counting efficiency of its lung counting system. The calibration of the system is performed using the Lawrence Livermore National Laboratory (LLNL) torso phantom; however, the effect of respiratory motion cannot be accounted for using these phantoms. When measuring an internal deposition in the lungs of a subject, respiration causes a change in the volume of the lungs and the thoracic cavity and introduces a variable distance between the lungs and the detectors. These changes may have an impact on the counting efficiency and may need to be considered during a measurement. In this study, the HML has simulated the respiration motion using a 4D non-uniform rational b-spline (NURBS)-based Cardiac-Torso (NCAT) phantom and determined the impact of that motion on the counting efficiency of their lung counting system during measurement. The respiratory motion was simulated by a 16 timeframe cycled 4D NURBS-based NCAT phantom developed at the Department of Biomedical Engineering and Radiology, University of North Carolina. The counting efficiency of the four germanium detectors comprising the HML lung counting system was obtained using MCNPX version 2.6E for photon energies between 17 and 1,000 keV. The amount of uncertainty due to the breathing motion was estimated by looking at the efficiency bias, which was highest at low photon energies as expected due to attenuation and geometry effects. Also, to reduce the influence of the detectors' positioning, an array was calculated by adding the individual detector tallies for a given energy and timeframe. For photon energies of 40 keV and higher, the array efficiency bias showed an underestimation of about 5%. If compared to other parameters already studied by the HML, this value demonstrates the insignificant impact of the breathing motion.**
Health Phys. 107(6):564–569; 2014

Key words: lungs, human; medical radiation; phantom; radiation protection

INTRODUCTION

Since 1995 (Kramer and Burns 1995), the Human Monitoring Laboratory (HML) in Canada has looked at a variety of parameters that can affect the counting efficiency of its lung counting system, which measures the internally deposited radioactivity in the lungs. Parameters like lung volume (Kramer and Capello 2005), lung deposition patterns (Kramer and Hauck 1999), and variability in the chest wall thickness profile (Kramer et al. 2000) have already been studied by the HML.

Currently, the HML lung counting system uses the Lawrence Livermore National Laboratory (LLNL) torso phantom (Griffith et al. 1978) and the Japanese Atomic Energy Research Institute (JAERI) realistic torso phantom (Shirotani 1988) for calibration purposes. However, the effect of respiratory motion cannot be simulated using these phantoms.

When measuring the internally deposited activity in the lungs of a subject, respiration causes a change in the volume of the lungs and thoracic cavity, a change of the lungs' densities due to inhaled air, and makes the distance between the chest surface and the detectors variable. These various factors may have an impact on the counting efficiency (and the estimated lung burden) and may need to be considered when calibrating a lung counting system or making an estimate of activity in a potentially contaminated person.

The density change of the lung due to inhaled air was assessed by the Institute of Radiation Research at the Karlsruhe Institute of Technology (Hegenbart and Breustedt 2010) in Germany. They obtained an increase in the counting efficiency of their detector array by 3% for a density change of 0.077 g cm^{-3} and a decrease of 6% in the counting efficiency for a density change of 0.177 g cm^{-3}. For a density change ranging from 0.294 to 0.360 g cm^{-3}, the change in the detector counting efficiency was about ± 1%. Hegenbart and Breustedt (2010) concluded that for an awake sitting male adult, the expected influence on lung counting efficiency caused by density fluctuations is marginal and can be neglected.

In this study, the HML has simulated the change in lung volume, the deformation of the chest, and the changes

*Radiation Protection Bureau, 775 Brookfield Road, Ottawa, Ontario, Canada; †2424 Erwin Road, Hock Plaza Suite 302, Durham, NC 27705.

The authors declare no conflicts of interest.

For correspondence contact: Marilyn Tremblay, Radiation Protection Bureau, 775 Brookfield Road, Ottawa, Ontario, Canada, or email at **marilyn.tremblay@hc-sc.gc.ca**.

(*Manuscript accepted* 6 *May* 2014)
0017-9078/14/0

DOI: 10.1097/HP.0000000000000156

in the distance between the detector and chest surface due to breathing using a 4D non-uniform rational b-spline (NURBS)-based Cardiac-Torso (NCAT) phantom (Segars and Tsui 2009). This study determined the impact of that motion on the counting efficiency of the lung counting system during a measurement and the effect it may have on the activity estimate.

MATERIALS AND METHODS

The Simulations

Monte Carlo simulations were performed with the Monte Carlo N-Particle Transport Code System X version 2.6E (Pelowitz 2005), known as MCNPX. It is a general purpose program that can be used for neutron, photon, electron, or coupled particles, although this work only makes use of the photon transport capabilities. It has been used for many applications, such as detection technology, shielding design, medical physics, radiation protection and shielding, nuclear safeguards, oil well logging, etc.

The 4D NURBS-based Cardiac-Torso (NCAT) phantom was developed at the Department of Biomedical Engineering and Department of Radiology, University of North Carolina, to model the respiratory motion of a human. It was originally developed to provide a realistic and flexible model of the human anatomy and physiology for use of image reconstruction methods and to study the effects of anatomical variation and patient motion in nuclear medicine research. NURBS surfaces were used to construct the organ shapes (diaphragm, heart, ribs, and lungs) in the NCAT phantom using the three-dimensional Visible Human Computed Tomography (CT) dataset as their basis. NURBS surfaces can be altered easily to model anatomical variations and patient motion. The NCAT phantom was extended to four dimensions to model common patient motions such as the cardiac and respiratory motions using 4D tagged magnetic resonance imaging (MRI) data and 4D high-resolution respiratory-gated CT data, respectively (Segars and Tsui 2009).

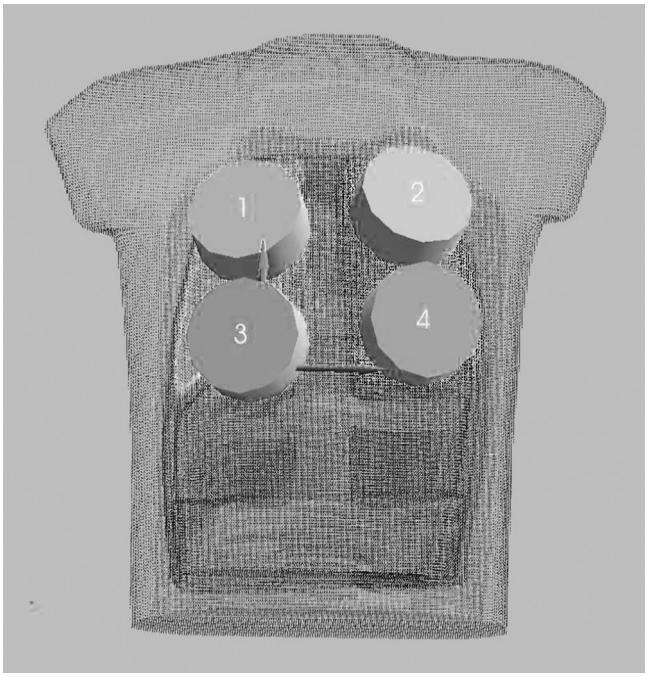

Fig. 1. Positioning of the four germanium detectors comprising the HML lung counting system on the LLNL torso phantom.

The NCAT respiratory motion was based on a set of respiratory-gated CT data from the University of Iowa taken from a normal volunteer at 5%, 40%, 75%, and 100% of his or her total lung capacity. By tracking landmark points on and within the respiratory structures, a general motion model for each organ and different regions inside the lungs was formulated. The motions were scaled down to correspond to normal tidal breathing (diaphragm motion of about 1 cm) and incorporated into the phantom. The motion was simulated by applying transformations to the control points defining the respiratory structures. The motion of the diaphragm was modeled by translating control points that define the left and right diaphragm surfaces. The heart, the stomach, and the spleen were translated rigidly up, down, backward, and forward with the movement of the diaphragm. The ribs were rotated about the axis through their costal necks to simulate their motion to expand and contract the chest.

These motions were set up to work in concert to produce a normal respiratory volume curve. Similar to the beating heart, the respiratory model was parameterized in terms of chest and diaphragm breathing so as to model different types of respiratory motions. With its realism and flexibility, the 4D NCAT cardiac and respiratory models provide useful tools to study the effects of motion and investigate 4D imaging techniques (Segars and Tsui 2009).

During respiration, the lungs inflate and deflate with changes in the volume of the thoracic cavity. The period of respiratory cycle for normal tidal breathing is 5 s, with inspiration lasting approximately 2 s and expiration lasting the remaining 3 s. The amount of volume change per lung for normal breathing is about 500 mL (Segars et al. 2001). The lung volumes of the altered phantom were compared to the lung volumes from the unaltered phantom to obtain the volume change in the lungs due to the diaphragm motion. The respiratory cycle was divided into 16 time frames to simulate the variations of different parameters describing the motion of the diaphragm, heart, thoracic cage, and lungs during the breathing cycle (Segars et al. 2001). The details of the 16 frames simulating the respiratory cycle are presented in Table 1.

The source included both lungs with a probability of photon generation in either lung being proportional to lung volume. The following energies were simulated

Table 1. Breathing details of the 16 frames simulating a respiratory cycle.

Frame	Time (s)	Heart phase index	Left ventricle contracting	Respiratory phase index	Inhaling
1	0.000	0.000	Fully relaxed	0.000	Full exhalation
2	0.312	0.312	89% contracted	0.062	14% inhaled
3	0.625	3.625	42% relaxed	0.125	27% inhaled
4	0.938	0.938	90% relaxed	0.188	41% inhaled
5	1.250	0.250	71% contracted	0.250	55% inhaled
6	1.562	0.562	33% relaxed	0.312	69% inhaled
7	1.875	0.875	81% relaxed	0.375	82% inhaled
8	2.188	0.188	53% contracted	0.438	96% inhaled
9	2.500	0.500	23% relaxed	0.500	8% exhaled
10	2.812	0.812	71% relaxed	0.562	20% exhaled
11	3.125	0.125	36% contracted	0.625	31% exhaled
12	3.438	0.438	13% relaxed	0.688	43% exhaled
13	3.750	0.750	61% relaxed	0.750	54% exhaled
14	4.062	0.062	18% contracted	0.812	66% exhaled
15	4.375	0.375	4% relaxed	0.875	77% exhaled
16	4.688	0.688	52% relaxed	0.938	89% exhaled

individually: 17, 20, 40, 60, 120, 240, 344, 660, and 1,000 keV. These energies were chosen to allow any energy to be interpolated but also to provide information specifically about ^{239}Pu, ^{241}Am, and natural uranium. As photons pass through the chest wall, they are attenuated to different degrees (based on their energy) by the tissues present; i.e., muscle, adipose, cartilage, bone (rib).

The number of photons generated varied from 10 million to 500 million depending on their energies. These photons interacted with the germanium in the detectors and were tallied individually so that an individual detector efficiency was obtained using MCNPX for each time frame. An array was calculated by simply adding the individual detector tallies for a given energy and time frame. The relative error varied from 0.004 to 0.028 for all simulations.

The four detectors were modeled after HML's lung counting detectors. Each of the four detectors is a P-type germanium crystal that is 85 mm in diameter and 30 mm in thickness; there is an inactive layer of germanium 700 μm thick on the surface. The entrance window is 0.76-mm carbon fiber and is 5 mm from the germanium crystal.

Fig. 1 shows the positioning of the four detectors on a LLNL torso phantom. The optimum counting position was determined to maximize the lung area covered by the placement of the four germanium detectors during lung counting (Ahmed et al. 2012). Detector #1 was placed above the upper portion of the right lung (upper right), detector #2 above the upper portion of the left lung (upper left), detector #3 above the lower portion of the right lung (lower right), and detector #4 above the lower portion of the left lung and above the heart (lower left).

The counting efficiency and its relative standard deviation for the four detectors comprising the HML's lung counting system were obtained using MCNPX for photon energies of 17, 20, 40, 60, 120, 240, 344, 660, and 1,000 keV.

The uncertainty introduced in the lung count due to the breathing motion can be estimated by calculating the bias. The following equation was used to express the effect of respiratory motion on the counting efficiency:

$$Bias(\%) = \frac{\left(\frac{\sum_{1}^{16} Efficiency}{16}\right) - Efficiency(\max)}{Efficiency(\max)} \times 100.$$

The maximum efficiency was used as the reference value to calculate the bias to best represent the calibration efficiency obtained with a physical phantom not considering the breathing motion.

RESULTS AND DISCUSSION

Table 2 presents the bias for the detector array and each individual detector for photons of 17, 20, 40, 60, 120, 240,

Table 2. Bias (%) for the detector array and each detector individually for photons of 17, 20, 40, 60, 120, 240, 344, 660, and 1000 keV during the 16 frames simulating the breathing cycle.

	Energy (keV)								
Detector	17	20	40	60	120	240	340	660	1,000
Array	−17	−10	−5.5	−5.1	−4.8	−4.7	−4.9	−4.9	−4.9
Detector 1	−20	−17	−7.4	−5.9	−4.8	−3.3	−2.5	−1.0	−0.9
Detector 2	−26	−17	−4.8	−3.1	−3.3	−1.8	−1.2	−1.1	−1.2
Detector 3	−18	−11	−10	−9.5	−8.7	−8.2	−7.9	−8.0	−7.6
Detector 4	−34	−30	−18	−16	−15	−13	−12	−11	−11

Table 3. Counting efficiency (count-per-second per photon-per-second) values of detector 1 calculated by MCNP.

	Detector 1								
Energy (keV)	17	20	40	60	120	240	340	660	1,000
Frame									
1	9.34×10^{-7}	1.94×10^{-5}	2.86×10^{-3}	4.81×10^{-3}	5.77×10^{-3}	4.67×10^{-3}	3.66×10^{-3}	2.35×10^{-3}	1.83×10^{-3}
2	9.05×10^{-7}	1.86×10^{-5}	2.77×10^{-3}	4.71×10^{-3}	5.65×10^{-3}	4.58×10^{-3}	3.60×10^{-3}	2.33×10^{-3}	1.82×10^{-3}
3	7.79×10^{-7}	1.63×10^{-5}	2.71×10^{-3}	4.62×10^{-3}	5.59×10^{-3}	4.57×10^{-3}	3.60×10^{-3}	2.33×10^{-3}	1.82×10^{-3}
4	6.36×10^{-7}	1.40×10^{-5}	2.62×10^{-3}	4.51×10^{-3}	5.52×10^{-3}	4.52×10^{-3}	3.58×10^{-3}	2.33×10^{-3}	1.83×10^{-3}
5	7.32×10^{-7}	1.58×10^{-5}	2.60×10^{-3}	4.47×10^{-3}	5.45×10^{-3}	4.48×10^{-3}	3.55×10^{-3}	2.32×10^{-3}	1.82×10^{-3}
6	6.19×10^{-7}	1.48×10^{-5}	2.55×10^{-3}	4.40×10^{-3}	5.37×10^{-3}	4.45×10^{-3}	3.54×10^{-3}	2.33×10^{-3}	1.82×10^{-3}
7	7.24×10^{-7}	1.52×10^{-5}	2.56×10^{-3}	4.39×10^{-3}	5.34×10^{-3}	4.45×10^{-3}	3.54×10^{-3}	2.32×10^{-3}	1.83×10^{-3}
8	6.08×10^{-7}	1.40×10^{-5}	2.49×10^{-3}	4.28×10^{-3}	5.24×10^{-3}	4.38×10^{-3}	3.49×10^{-3}	2.31×10^{-3}	1.81×10^{-3}
9	5.74×10^{-7}	1.36×10^{-5}	2.48×10^{-3}	4.28×10^{-3}	5.24×10^{-3}	4.39×10^{-3}	3.50×10^{-3}	2.31×10^{-3}	1.82×10^{-3}
10	7.26×10^{-7}	1.52×10^{-5}	2.56×10^{-3}	4.39×10^{-3}	5.34×10^{-3}	4.45×10^{-3}	3.54×10^{-3}	2.33×10^{-3}	1.83×10^{-3}
11	6.15×10^{-7}	1.48×10^{-5}	2.57×10^{-3}	4.42×10^{-3}	5.39×10^{-3}	4.46×10^{-3}	3.55×10^{-3}	2.33×10^{-3}	1.82×10^{-3}
12	7.86×10^{-7}	1.65×10^{-5}	2.62×10^{-3}	4.50×10^{-3}	5.48×10^{-3}	4.50×10^{-3}	3.56×10^{-3}	2.33×10^{-3}	1.83×10^{-3}
13	7.42×10^{-7}	1.56×10^{-5}	2.64×10^{-3}	4.57×10^{-3}	5.58×10^{-3}	4.57×10^{-3}	3.61×10^{-3}	2.35×10^{-3}	1.84×10^{-3}
14	8.08×10^{-7}	1.74×10^{-5}	2.77×10^{-3}	4.64×10^{-3}	5.59×10^{-3}	4.57×10^{-3}	3.61×10^{-3}	2.34×10^{-3}	1.83×10^{-3}
15	9.23×10^{-7}	1.81×10^{-5}	2.78×10^{-3}	4.71×10^{-3}	5.64×10^{-3}	4.59×10^{-3}	3.61×10^{-3}	2.33×10^{-3}	1.83×10^{-3}
16	8.56×10^{-7}	1.79×10^{-5}	2.76×10^{-3}	4.70×10^{-3}	5.66×10^{-3}	4.59×10^{-3}	3.60×10^{-3}	2.33×10^{-3}	1.82×10^{-3}

344, and 1,000 keV during the 16 frames simulating the breathing cycle.

In summary, the results for the array show an underestimation of the radioactivity by 17% and 10% at 17 keV and 20 keV, respectively, and a maximum underestimation of 5.5% for photon energies between 40 keV and 1,000 keV.

For the individual detectors, the radioactivity underestimations vary between 18% to 34% at 17 keV and between 11% to 30% at 20 keV. Between 40 keV and 100 keV, the underestimation of the radioactivity varies from 0.9% to 18%. The positioning of Detector #4 above the heart, falling off from the left lung, explains the lower efficiencies obtained for that detector (Table 6).

The following can be concluded:

- The bias values for the array and individual detectors are highest at low photon energies (17 keV and 20 keV) as expected due to attenuation and geometry effects;
- The gross difference between each individual detector efficiency shows that the use of individual detectors to determine whether a deposition is homogenous or

Table 4. Counting efficiency (count-per-second per photon-per-second) values of detector 2 calculated by MCNP.

	Detector 2								
Energy (keV)	17	20	40	60	120	240	340	660	1,000
Frame									
1	7.49×10^{-7}	1.60×10^{-5}	2.62×10^{-3}	4.46×10^{-3}	5.48×10^{-3}	4.48×10^{-3}	3.52×10^{-3}	2.27×10^{-3}	1.75×10^{-3}
2	7.78×10^{-7}	1.60×10^{-5}	2.66×10^{-3}	4.51×10^{-3}	5.54×10^{-3}	4.53×10^{-3}	3.56×10^{-3}	2.29×10^{-3}	1.77×10^{-3}
3	8.26×10^{-7}	1.65×10^{-5}	2.64×10^{-3}	4.46×10^{-3}	5.46×10^{-3}	4.48×10^{-3}	3.54×10^{-3}	2.29×10^{-3}	1.77×10^{-3}
4	7.42×10^{-7}	1.54×10^{-5}	2.63×10^{-3}	4.48×10^{-3}	5.47×10^{-3}	4.51×10^{-3}	3.57×10^{-3}	2.32×10^{-3}	1.79×10^{-3}
5	7.78×10^{-7}	1.64×10^{-5}	2.61×10^{-3}	4.45×10^{-3}	5.43×10^{-3}	4.51×10^{-3}	3.57×10^{-3}	2.32×10^{-3}	1.79×10^{-3}
6	6.36×10^{-7}	1.52×10^{-5}	2.54×10^{-3}	4.30×10^{-3}	5.24×10^{-3}	4.41×10^{-3}	3.51×10^{-3}	2.29×10^{-3}	1.79×10^{-3}
7	5.05×10^{-7}	1.26×10^{-5}	2.43×10^{-3}	4.19×10^{-3}	5.18×10^{-3}	4.37×10^{-3}	3.49×10^{-3}	2.29×10^{-3}	1.78×10^{-3}
8	6.05×10^{-7}	1.44×10^{-5}	2.51×10^{-3}	4.28×10^{-3}	5.24×10^{-3}	4.42×10^{-3}	3.53×10^{-3}	2.31×10^{-3}	1.80×10^{-3}
9	5.60×10^{-7}	1.38×10^{-5}	2.49×10^{-3}	4.26×10^{-3}	5.24×10^{-3}	4.42×10^{-3}	3.53×10^{-3}	2.31×10^{-3}	1.80×10^{-3}
10	5.06×10^{-7}	1.27×10^{-5}	2.44×10^{-3}	4.20×10^{-3}	5.19×10^{-3}	4.38×10^{-3}	3.50×10^{-3}	2.29×10^{-3}	1.78×10^{-3}
11	6.24×10^{-7}	1.49×10^{-5}	2.53×10^{-3}	4.30×10^{-3}	5.25×10^{-3}	4.40×10^{-3}	3.51×10^{-3}	2.28×10^{-3}	1.78×10^{-3}
12	6.30×10^{-7}	1.47×10^{-5}	2.50×10^{-3}	4.33×10^{-3}	5.32×10^{-3}	4.44×10^{-3}	3.53×10^{-3}	2.30×10^{-3}	1.78×10^{-3}
13	7.09×10^{-7}	1.46×10^{-5}	2.53×10^{-3}	4.35×10^{-3}	5.34×10^{-3}	4.44×10^{-3}	3.52×10^{-3}	2.29×10^{-3}	1.78×10^{-3}
14	8.05×10^{-7}	1.62×10^{-5}	2.61×10^{-3}	4.43×10^{-3}	5.42×10^{-3}	4.46×10^{-3}	3.52×10^{-3}	2.29×10^{-3}	1.76×10^{-3}
15	9.42×10^{-7}	1.83×10^{-5}	2.69×10^{-3}	4.48×10^{-3}	5.44×10^{-3}	4.47×10^{-3}	3.52×10^{-3}	2.28×10^{-3}	1.76×10^{-3}
16	7.92×10^{-7}	1.63×10^{-5}	2.62×10^{-3}	4.45×10^{-3}	5.46×10^{-3}	4.48×10^{-3}	3.53×10^{-3}	2.27×10^{-3}	1.76×10^{-3}

Table 5. Counting efficiency (count-per-second per photon-per-second) values of detector 3 calculated by MCNP.

	Detector 3								
Energy (keV)	17	20	40	60	120	240	340	660	1,000
Frame									
1	8.21×10^{-6}	7.26×10^{-5}	3.78×10^{-3}	5.95×10^{-3}	6.90×10^{-3}	5.32×10^{-3}	4.09×10^{-3}	2.55×10^{-3}	1.94×10^{-3}
2	8.02×10^{-6}	6.92×10^{-5}	3.62×10^{-3}	5.74×10^{-3}	6.70×10^{-3}	5.19×10^{-3}	4.01×10^{-3}	2.50×10^{-3}	1.91×10^{-3}
3	6.40×10^{-6}	6.44×10^{-5}	3.79×10^{-3}	6.04×10^{-3}	7.01×10^{-3}	5.41×10^{-3}	4.18×10^{-3}	2.61×10^{-3}	1.99×10^{-3}
4	6.41×10^{-6}	6.42×10^{-5}	3.90×10^{-3}	6.24×10^{-3}	7.27×10^{-3}	5.61×10^{-3}	4.32×10^{-3}	2.69×10^{-3}	2.05×10^{-3}
5	9.21×10^{-6}	8.04×10^{-5}	4.14×10^{-3}	6.53×10^{-3}	7.53×10^{-3}	5.79×10^{-3}	4.46×10^{-3}	2.79×10^{-3}	2.12×10^{-3}
6	7.71×10^{-6}	7.60×10^{-5}	4.31×10^{-3}	6.83×10^{-3}	7.87×10^{-3}	6.05×10^{-3}	4.66×10^{-3}	2.91×10^{-3}	2.20×10^{-3}
7	7.57×10^{-6}	7.93×10^{-5}	4.52×10^{-3}	7.13×10^{-3}	8.18×10^{-3}	6.26×10^{-3}	4.81×10^{-3}	3.00×10^{-3}	2.27×10^{-3}
8	6.21×10^{-6}	6.81×10^{-5}	4.30×10^{-3}	6.86×10^{-3}	7.91×10^{-3}	6.10×10^{-3}	4.70×10^{-3}	2.95×10^{-3}	2.24×10^{-3}
9	6.17×10^{-6}	6.81×10^{-5}	4.32×10^{-3}	6.89×10^{-3}	7.95×10^{-3}	6.13×10^{-3}	4.72×10^{-3}	2.96×10^{-3}	2.24×10^{-3}
10	7.88×10^{-6}	8.14×10^{-5}	4.53×10^{-3}	7.13×10^{-3}	8.18×10^{-3}	6.26×10^{-3}	4.80×10^{-3}	3.00×10^{-3}	2.27×10^{-3}
11	8.36×10^{-6}	8.14×10^{-5}	4.46×10^{-3}	7.03×10^{-3}	8.08×10^{-3}	6.18×10^{-3}	4.74×10^{-3}	2.95×10^{-3}	2.23×10^{-3}
12	9.26×10^{-6}	8.04×10^{-5}	4.17×10^{-3}	6.59×10^{-3}	7.59×10^{-3}	5.84×10^{-3}	4.49×10^{-3}	2.80×10^{-3}	2.13×10^{-3}
13	8.70×10^{-6}	7.89×10^{-5}	4.14×10^{-3}	6.53×10^{-3}	7.53×10^{-3}	5.79×10^{-3}	4.46×10^{-3}	2.77×10^{-3}	2.10×10^{-3}
14	5.70×10^{-6}	5.95×10^{-5}	3.77×10^{-3}	6.02×10^{-3}	7.00×10^{-3}	5.43×10^{-3}	4.18×10^{-3}	2.61×10^{-3}	2.00×10^{-3}
15	7.88×10^{-6}	7.19×10^{-5}	3.81×10^{-3}	6.02×10^{-3}	6.99×10^{-3}	5.38×10^{-3}	4.15×10^{-3}	2.58×10^{-3}	1.96×10^{-3}
16	7.84×10^{-6}	6.90×10^{-5}	3.65×10^{-3}	5.80×10^{-3}	6.75×10^{-3}	5.23×10^{-3}	4.04×10^{-3}	2.52×10^{-3}	1.92×10^{-3}

heterogeneous may be problematic. This is a topic that requires further study; and

- The bias results obtained for the array are considerably smaller than the values for an individual detector. As already stated in previous studies, the accuracy of measurement depends on the positioning of the detectors relative to the phantom or the person counted (Hegenbart and Breustedt 2010). Ideally, the operator needs to reproduce the same detector position for the calibration measurements with the phantom and for each test person measurement, which is not always possible.

The data show that a detector array will minimize the uncertainties arising from the positioning of the detectors, the geometry of the lung deposition, and respiratory motion.

Other studies made previously at the HML have obtained an overestimation for the activity in the lung as high as 63% at 17 keV and 41% at 60 keV for a lung size variation of about 9,000 mL (Kramer and Capello 2005). For this study, a variation of lung volume of about 500 mL was simulated, which corresponds to normal breathing. Small bias values were obtained, as expected.

Table 6. Counting efficiency (count-per-second per photon-per-second) values of detector 4 calculated by MCNP.

	Detector 4								
Energy (keV)	17	20	40	60	120	240	340	660	1,000
Frame									
1	2.06×10^{-6}	2.07×10^{-5}	2.29×10^{-3}	3.96×10^{-3}	4.92×10^{-3}	4.10×10^{-3}	3.26×10^{-3}	2.14×10^{-3}	1.66×10^{-3}
2	2.25×10^{-6}	2.40×10^{-5}	2.39×10^{-3}	4.03×10^{-3}	4.94×10^{-3}	4.13×10^{-3}	3.28×10^{-3}	2.15×10^{-3}	1.67×10^{-3}
3	2.51×10^{-6}	2.59×10^{-5}	2.50×10^{-3}	4.24×10^{-3}	5.20×10^{-3}	4.32×10^{-3}	3.41×10^{-3}	2.23×10^{-3}	1.73×10^{-3}
4	3.24×10^{-6}	3.36×10^{-5}	2.79×10^{-3}	4.62×10^{-3}	5.60×10^{-3}	4.61×10^{-3}	3.64×10^{-3}	2.37×10^{-3}	1.82×10^{-3}
5	4.39×10^{-6}	4.16×10^{-5}	3.01×10^{-3}	4.97×10^{-3}	6.01×10^{-3}	4.90×10^{-3}	3.85×10^{-3}	2.49×10^{-3}	1.91×10^{-3}
6	4.50×10^{-6}	4.50×10^{-5}	3.27×10^{-3}	5.30×10^{-3}	6.37×10^{-3}	5.15×10^{-3}	4.04×10^{-3}	2.60×10^{-3}	2.00×10^{-3}
7	4.68×10^{-6}	4.55×10^{-5}	3.32×10^{-3}	5.47×10^{-3}	6.59×10^{-3}	5.32×10^{-3}	4.18×10^{-3}	2.68×10^{-3}	2.06×10^{-3}
8	5.37×10^{-6}	5.10×10^{-5}	3.50×10^{-3}	5.70×10^{-3}	6.80×10^{-3}	5.46×10^{-3}	4.28×10^{-3}	2.73×10^{-3}	2.10×10^{-3}
9	5.22×10^{-6}	5.13×10^{-5}	3.52×10^{-3}	5.73×10^{-3}	6.83×10^{-3}	5.49×10^{-3}	4.30×10^{-3}	2.74×10^{-3}	2.10×10^{-3}
10	4.74×10^{-6}	4.61×10^{-5}	3.35×10^{-3}	5.50×10^{-3}	6.61×10^{-3}	5.34×10^{-3}	4.19×10^{-3}	2.69×10^{-3}	2.07×10^{-3}
11	4.16×10^{-6}	4.27×10^{-5}	3.16×10^{-3}	5.13×10^{-3}	6.19×10^{-3}	5.04×10^{-3}	3.96×10^{-3}	2.56×10^{-3}	1.97×10^{-3}
12	4.06×10^{-6}	3.88×10^{-5}	2.97×10^{-3}	4.95×10^{-3}	6.02×10^{-3}	4.90×10^{-3}	3.86×10^{-3}	2.49×10^{-3}	1.91×10^{-3}
13	3.15×10^{-6}	3.30×10^{-5}	2.78×10^{-3}	4.64×10^{-3}	5.64×10^{-3}	4.65×10^{-3}	3.68×10^{-3}	2.40×10^{-3}	1.84×10^{-3}
14	2.05×10^{-6}	2.26×10^{-5}	2.43×10^{-3}	4.17×10^{-3}	5.17×10^{-3}	4.30×10^{-3}	3.41×10^{-3}	2.24×10^{-3}	1.73×10^{-3}
15	2.36×10^{-6}	2.58×10^{-5}	2.45×10^{-3}	4.11×10^{-3}	5.02×10^{-3}	4.18×10^{-3}	3.32×10^{-3}	2.17×10^{-3}	1.68×10^{-3}
16	2.12×10^{-6}	2.27×10^{-5}	2.36×10^{-3}	4.00×10^{-3}	4.94×10^{-3}	4.13×10^{-3}	3.28×10^{-3}	2.14×10^{-3}	1.66×10^{-3}

Table 7. Counting efficiency (count-per-second per photon-per-second) values for the virtual four germanium detector array.

	Array								
Energy (keV)	17	20	40	60	120	240	340	660	1,000
Frame									
1	1.20×10^{-5}	1.29×10^{-4}	1.15×10^{-2}	1.92×10^{-2}	2.31×10^{-2}	1.8×10^{-2}	1.45×10^{-2}	9.32×10^{-3}	7.19×10^{-3}
2	1.20×10^{-5}	1.28×10^{-4}	1.14×10^{-2}	1.90×10^{-2}	2.28×10^{-2}	1.84×10^{-2}	1.45×10^{-2}	9.27×10^{-3}	7.17×10^{-3}
3	1.05×10^{-5}	1.23×10^{-4}	1.16×10^{-2}	1.94×10^{-2}	2.33×10^{-2}	1.88×10^{-2}	1.47×10^{-2}	9.47×10^{-3}	7.31×10^{-3}
4	1.10×10^{-5}	1.27×10^{-4}	1.19×10^{-2}	1.99×10^{-2}	2.39×10^{-2}	1.92×10^{-2}	1.51×10^{-2}	9.71×10^{-3}	7.49×10^{-3}
5	1.51×10^{-5}	1.54×10^{-4}	1.24×10^{-2}	2.04×10^{-2}	2.44×10^{-2}	1.97×10^{-2}	1.54×10^{-2}	9.92×10^{-3}	7.64×10^{-3}
6	1.35×10^{-5}	1.51×10^{-4}	1.27×10^{-2}	2.08×10^{-2}	2.49×10^{-2}	2.01×10^{-2}	1.57×10^{-2}	1.01×10^{-3}	7.81×10^{-3}
7	1.35×10^{-5}	1.53×10^{-4}	1.28×10^{-2}	2.12×10^{-2}	2.53×10^{-2}	2.04×10^{-2}	1.60×10^{-2}	1.03×10^{-3}	7.95×10^{-3}
8	1.28×10^{-5}	1.47×10^{-4}	1.28×10^{-2}	2.11×10^{-2}	2.52×10^{-2}	2.04×10^{-2}	1.60×10^{-2}	1.03×10^{-3}	7.96×10^{-3}
9	1.25×10^{-5}	1.47×10^{-4}	1.28×10^{-2}	2.12×10^{-2}	2.53×10^{-2}	2.04×10^{-2}	1.61×10^{-2}	1.03×10^{-3}	7.97×10^{-3}
10	1.39×10^{-5}	1.55×10^{-4}	1.29×10^{-2}	2.12×10^{-2}	2.53×10^{-2}	2.04×10^{-2}	1.60×10^{-2}	1.03×10^{-3}	7.95×10^{-3}
11	1.38×10^{-5}	1.54×10^{-4}	1.27×10^{-2}	2.09×10^{-2}	2.49×10^{-2}	2.01×10^{-2}	1.58×10^{-2}	1.01×10^{-3}	7.81×10^{-3}
12	1.47×10^{-5}	1.50×10^{-4}	1.23×10^{-2}	2.04×10^{-2}	2.44×10^{-2}	1.97×10^{-2}	1.55×10^{-2}	9.93×10^{-3}	7.66×10^{-3}
13	1.33×10^{-5}	1.42×10^{-4}	1.21×10^{-2}	2.01×10^{-2}	2.41×10^{-2}	1.95×10^{-2}	1.53×10^{-2}	9.81×10^{-3}	7.56×10^{-3}
14	9.37×10^{-5}	1.16×10^{-4}	1.16×10^{-2}	1.93×10^{-2}	2.32×10^{-2}	1.88×10^{-2}	1.47×10^{-2}	9.48×10^{-3}	7.32×10^{-3}
15	1.21×10^{-5}	1.34×10^{-4}	1.17×10^{-2}	1.93×10^{-2}	2.31×10^{-2}	1.86×10^{-2}	1.46×10^{-2}	9.36×10^{-3}	7.24×10^{-3}
16	1.16×10^{-5}	1.26×10^{-4}	1.14×10^{-2}	1.90×10^{-2}	2.28×10^{-2}	1.84×10^{-2}	1.45×10^{-2}	9.27×10^{-3}	7.17×10^{-3}

These results show that the change in the volume of the lungs and the thoracic cavity caused by the motion of the diaphragm, the heart, the stomach, the spleen, and the rotation of the ribs during normal tidal breathing does not have a significant influence on the array counting efficiency of the HML lung counting system.

CONCLUSION

The HML has used a 4D non-uniform rational b-spline (NURBS)-based Cardiac-Torso (NCAT) phantom to model the respiratory motion of a human and determine the impact of that motion on the counting efficiency of the lung counting system during a real measurement. The results obtained for the four detector array used in the HML lung counting system with photon energies of 17 keV and 20 keV indicate an underestimation of the radioactivity by 17% and 10%, respectively. For photon energies of 40 keV and higher, the results demonstrate a maximum underestimation of the radioactivity by 5.5%.

If compared with other parameters already studied by the HML (lung volume, deposition patterns, etc.), these values show that breathing is a small contribution to the overall uncertainty in lung counting and can be neglected. The use of a 4D NCAT phantom to simulate the respiratory motion is unnecessary when developing calibration factors for a lung counting system; however, it is worth remembering that the close geometry used during the calibration process introduces a systematic bias that results in all lung burdens being underestimated by a few percent.

REFERENCES

Ahmed SA, Hauck BM, Kramer GH. Lung counting: comparison of detector performance with a four detector array. Radiat Protect Dosim 151:262–266; 2012.

Griffith RV, Dean PN, Anderson AL, Fisher JC. Tissue equivalent torso phantom for intercalibration of in vivo transuranic nuclide counting facilities. In: Advances in radiation monitoring, Proceedings of an International Atomic Energy Agency Conference. Vienna: IAEA; IAEA-SM-229/56, 4493–504; 1978.

Hegenbart L, Breustedt B. A new position recording system for the partial-body counter at KIT. Radioprotect Dosim 144: 389–392; 2010.

Kramer GH, Burns LC. Effect of radionuclide distributions on lung counting efficiency. Radiat Protect Dosim 61:145–147; 1995.

Kramer GH, Hauck BM. The effect of lung deposition patterns on the activity estimate obtained from a large area germanium detector lung counter. Health Phys 77:24–32; 1999.

Kramer GH, Burns LC. Evaluation of the effect of the chest wall thickness, tissue composition, and photon energy on the quantity muscle-equivalent chest-wall-thickness by Monte Carlo simulation. Radioprotect Dosim 82:115–124; 1999.

Kramer GH, Crowley P, Burns LC. The uncertainty in the activity estimate from a lung count due to the variability in chest wall thickness profile. Health Phys 78:739–743; 2000.

Kramer GH, Capello K. Effect of lung volume on counting efficiency: a Monte Carlo investigation. Health Phys 88:357–363; 2005.

Pelowitz DB. MCNPXTM user's manual. Los Alamos, NM: Los Alamos National Laboratory; LA-CP-05-0369; 2005.

Segars WP, Tsui BMW. MCAT to XCAT: The evolution of 4-D computerized phantoms for imaging research. IEEE Trans Nucl Sci 97(12):1954–1968; 2009.

Segars WP, Lalush DS, Tsui BMW. Modeling respiratory mechanics in the MCAT and spline-based MCAT phantoms. IEEE Trans Nucl Sci 48(1):89–97; 2001.

Shirotani T. Realistic torso phantom for calibration on in vivo transuranic-nuclide counting facilities. J Nucl Sci and Tech 25:875–883; 1988.

■■